Multi-view light-sheet microscope for rapid *in toto* imaging

Uros Krzic[1], Stefan Gunther[1,2], Timothy E Saunders[1,2], Sebastian J Streichan[1], and Lars Hufnagel[1]*

1. Cell Biology and Biophysics Unit
2. Genome Biology Unit
European Molecular Biology Laboratory, Meyerhofstr. 1, D-69117 Heidelberg, Germany

* Correspondence should be sent to hufnagel@embl.de

U.K. and L.H. designed and built the microscope software and hardware. U.K., S.G. and T.S. performed the experiments. U.K., S.G., T.S. and S.S. performed data analysis, quantification and visualization. All authors contributed to the writing of the manuscript.

We present a multi-view selective-plane illumination microscope (MuVi-SPIM), comprised of two detection and illumination objective lenses, that allows rapid *in toto* fluorescence imaging of biological specimens with subcellular resolution. The fixed geometrical arrangement of the imaging branches enables multi-view data fusion in real-time. The high speed of MuVi-SPIM enables faithful tracking of nuclei and cell shape changes, which we demonstrate by *in toto* imaging the embryonic development of *Drosophila melanogaster*.

Developmental processes are highly dynamic and span many temporal and spatial scales. During development, cells must integrate and respond to a multitude of biochemical and biophysical signals; for example, changes in intracellular signaling networks, cytoskeleton remodeling, cell shape changes, long-range signaling, and tissue remodeling[1–3]. A whole-embryo view of morphogenesis with sub-cellular resolution is essential to unravel the interconnected dynamics at the varying scales of development, from interactions within cells to those acting across the whole embryo. Bridging scales from the sub-micron to the millimeter range with temporal resolution of several seconds (combined with total imaging time of several hours) not only poses tremendous challenges for modern microscopy methods but also requires powerful computational approaches for data handling, processing and image analysis.

The recently rediscovered selective plane illumination microscopy (SPIM) has emerged as a powerful technique for biological imaging[4–7]. It has proven its potential with specimens ranging from single cells to entire animals[8–10] and has been successfully combined with other modern microscopy methods[11,12]. SPIM generates optically-sectioned images of a fluorescent specimen by illuminating only a section of the specimen with a thin light-sheet, while the emitted fluorescence is collected by a wide-field microscope that is oriented perpendicular to the light-sheet (Supplementary Fig. 1). Since SPIM only illuminates the section that is imaged, the biological specimen is exposed to an orders-of-magnitude lower light dose than in a laser-scanning confocal microscope, when hundreds of optical sections are imaged[6]. This makes SPIM especially well placed for imaging of entire organisms with sizes up to a few millimetres.

At macroscopic scales, however, light scattering and absorption in tissues limit image quality, in particular for opaque specimens. Previously, to circumvent this issue, rotation of large specimens has been used to gain detailed images from multiple directions[13,14]. Moreover, specimen rotation was shown to improve resolution by reducing the effects of an anisotropic point-spread function (PSF), standard to most microscopes (SPIM included)[13,15].

Multi-directional imaging by specimen rotation suffers from three severe drawbacks. First, as position and orientation of the axis of rotation relative to the specimen is difficult to determine with high precision, multiple images obtained by specimen rotation are inherently misaligned[15]. This problem has previously been tackled by data-driven image registration algorithms, often necessitating the use of fiducial markers[14]. Second, due to the soft agarose embedding of specimens required for high quality imaging, rotation is often slower than the biological dynamics preventing the synthesis of data from multiple views into a single three-dimensional intensity distribution. Third, since the quality of marker-free image-based registration decreases rapidly when there is insufficient overlap between neighboring views, a considerable number of viewing directions have to be acquired to yield reliable results, exacerbating the drawbacks in time-resolution, while increasing photobleaching and toxicity. These problems are important reasons why multi-view microscopy is yet to become a widely used technique in biology.

To address the above challenges, we have built a novel optical setup together with an efficient and reliable data processing pipeline that exploits the full potential of multi-view SPIM microscopy. Our approach significantly reduces the need for specimen rotation and is therefore robust, fast and easy to use. MuVi-SPIM allows, for the first time, the rapid imaging of large fluorescent specimens from multiple directions over biologically relevant timescales, and reconstruction of the images into a single high-quality image in real-time. MuVi-SPIM uses two illumination and two detection objective lenses that are focused onto a specimen from four different directions, along two perpendicular axes (Fig. 1a). A specialized alignment procedure (see Supplementary Protocol 1) ensures that both detection objective lenses are focused onto a common focal plane, which is in turn illuminated by the two light-sheets. Each light-sheet is generated by scanning a Gaussian beam with constant

velocity across the specimen[8] through either of the illumination objective lenses (Fig. 1b-c). Three-dimensional images are accumulated by recording a series of sections while the specimen is moved through the light-sheet by a fast piezo stage. The two illumination and detection lenses form four distinct illumination/detection pairs (called imaging branches, see Fig. 1d-e), each producing a three-dimensional image. The four resulting images are sufficient to yield a three-dimensional all-around view of a specimen without rotation. Furthermore, since both detection arms are used simultaneously, MuVi-SPIM has an effective light efficiency that is twice as high as that of other SPIM implementations. The microscope allows flexibility in the definition of the temporal sequence of stage motion, light-sheet illumination, and detection: enabling tailoring of the operation to biological dynamics under study. Although MuVi-SPIM in principle allows illumination of the sample simultaneously from both sides (this mode would roughly half the imaging time), it was shown that this tends to reduce the overall image quality due to scattering[16]. Here, we implemented a sequential mode of operation where each camera records a complete three-dimensional stack from one light sheet first before switching to the other light sheet. Real-time electronics ensure the precise timing of all microscopy parts. Due to the mechanical stability of the specimen mounting from below (Supplementary Fig. 2), MuVi-SPIM is capable of imaging three-dimensional images with 100 sections per second (see Methods and Supplementary Note 2 for detailed description of the microscope setup).

The four views obtained by the four imaging branches represent the same fluorophore distribution in the specimen and are therefore linked to each other by a set of geometrical transformations. Translation alone was shown to be insufficient to register multi-view SPIM images due to imaging-angle dependant image deformations[15], most notably image scaling (mismatch in magnifications of the two detection arms), image rotation around the detection axis (rotationally misaligned cameras) and skew (piezo translation not parallel to the detection axis). We have therefore used a three-dimensional affine transformation model, which covers all first-order image transformations including the three listed above, to transform the four multi-view views into a common coordinate system. Parameters of the affine transformation can be efficiently obtained with a use of a diagnostic specimen, consisting of fluorescent beads dispersed in agarose. Since the transformation parameters are defined solely by the four optical arms, the parameters obtained with the use of the diagnostic specimen remain valid after the specimen is replaced. We have also assessed the stability of the MuVi-SPIM setup by imaging dispersed fluorescent beads every 30 minutes over a 16 hour period. During this period, the affine transformation parameters linking the four views drifted less than the equivalent of 0.5 μm relative to each other (Supplementary Fig. 3). The geometric relations between the four different views are thus a fixed property of the microscope and remain static even for long imaging times. Hence the parameters defining the relations between the four views, in our case affine transformation coefficients, can be determined prior to the experiment and will remain valid for any number of subsequent images and/or following specimen exchange.

In order to construct a single image of fluorophore distribution in a specimen (rather than four independent images) all four images are first transformed into a common coordinate system using affine transformation parameters derived from the bead analysis. The four transformed views are then combined to synthesize a single image as a weighted average (Fig. 1e, see Supplementary Figs. 4 and 5 and Methods for further details); higher weight is given to the parts of every view where the image quality is expected to be best. Geometric transformation and synthesis of four 550 megapixel three-dimensional images (2,560 x 2,160 x 101) normally requires around three seconds, which is less than it typically takes to acquire such a multi-view image set; MuVi-SPIM can process raw data to high-quality fused images in real-time with frame rates of up to 30 two-dimensional sections per second. Importantly, unlike in previous multi-view SPIM implementations, the quality of the MuVi-SPIM image registration is independent of image content - it performs equally well with specimens that produce images with low intensity or contrast.

We demonstrate the potential of the MuVi-SPIM for *in toto* imaging of morphogenetic processes by recording nuclear positions and cell shapes in the highly dynamic embryonic development of *Drosophila melanogaster*. The *Drosophila* embryo undergoes many rapid and large scale morphological processes, such as fast nuclear cleavage divisions in the early embryo, ventral furrow formation, germ band extension, and dorsal closure. Previous studies were restricted to limited spatial regions of the embryo and only individual morphological process could be imaged with sub-cellular resolution. A comprehensive view of the interplay of these processes is thus still lacking. Since MuVi-SPIM yields quasi-instantaneous three-dimensional fluorophore distributions it enables us to reconstruct an image of the entire embryo without any mismatches between parts from different imaging branches, see Fig. 2a and Supplementary Videos 1-4.

To test the imaging speed and quality of our embryo image reconstruction we investigated nuclear division in early *Drosophila* development. In the *Drosophila* blastoderm, mitotic divisions occur up to every eight minutes and take less than one minute to complete[17]. The imaging time for a complete embryo on MuVi-SPIM was around 20 seconds. Using fused MuVi-SPIM images of his2Av-mCherry expressing embryos (Fig. 2a), we could robustly segment (see Methods) and count nuclei from cycle 10 to 14 (Fig. 2b and Supplementary Video 5). It also enables faithful reconstruction of cell lineages by tracking nuclei, even through several rounds of division (Fig. 2c,d and Supplementary Video 6), and allows for the quantification of nuclei dynamics (Supplementary Fig. 6, Supplementary Video 7, Methods and Supplementary Note 6 for details). To demonstrate the potential of MuVi-SPIM for imaging of dense tissues undergoing morphological transformations we recorded *in toto Drosophila* embryo development starting from early cycle 14 for fifteen hours (including through gastrulation) using his2Av-mCherry expressing embryos at high temporal resolution (10 seconds imaging time for full embryo, at 30 second intervals), Supplementary Video 8. Cells from a same region in the ventral ectoderm were selected and tracked through five hours of development along with their daughter cells (see Methods for tracking algorithm details). These cells were first arranged along a straight line, then formed a part of a *rosette*, later intercolated and finally underwent two rounds of cell divisions. Despite the large-scale morphological motion, these cells (and their progeny) remained closely associated. Example tracks are shown in Supplementray Fig. 7 and Supplementary Video 9. This provides a powerful approach to understanding the dynamics of tissue development, e.g. tracing cell fate decisions in the *in vivo* context of the tissue.

While specimen rotation is not required for complete all-around imaging in MuVi-SPIM, it can still lead to improved image quality. The point-spread function of any standard microscope is elongated along the optical axis of the detection objective lens; the microscope's axial resolution is always several times worse than its lateral resolution. In MuVi-SPIM, resolution along the detection axis is approximately five times worse than perpendicularly to it (with a numerical aperture of 0.8). As demonstrated above, this presents no problem when structures of interest are bigger than the microscope's axial resolution. However, when structures are smaller and/or spaced by distances shorter than the microscope's axial resolution, anisotropic resolution makes analysis of three-dimensional images difficult. For example, on conventional fluorescence microscopes (including SPIM), fluorescent membranes aligned parallel to the long axis of the PSF yield good contrast while perpendicular membranes appear dim, blurred and difficult to resolve (Supplementary Fig. 8).

Shape transformations of tissues, tissue migration and remodeling are omnipresent processes during embryonic development[3]. The quantification of cell shape changes is an important step to connect the intra-cellular dynamics with large-scale changes. But, to overcome the limits of the anisotropic resolution, as in other SPIM implementations, the specimen can be rotated in MuVi-SPIM during imaging. After four images of a multi-view set are recorded, the specimen is rotated for 90^{o} and another image set is acquired. Hence, the total time taken to complete one imaging cycle is

approximately doubled. It is noteworthy that despite this, eight-view image sets are collected at least four times faster than in a conventional SPIM.

Fig. 2e shows a MuVi-SPIM image of cell membranes in a *Drosophila* embryo during early cycle 14 expressing Gap43-mCherry (see Methods and Supplementary Notes 4-6 for experimental and image analysis details). To acquire eight images (two MuVi-SPIM datasets, four images each) of the entire embryo took 43 seconds, compared to timescales of minutes that were typical in previous attempts to view *Drosophila* embryo in three-dimensions using SPIM. Each of the two MuVi-SPIM image sets was fused as described above, and the resulting images were registered using image cross-correlation[18] (see Methods). As the two intermediate fused images contain much more information than the any of the initial eight recordings, this registration step converges reliably and fast. Moreover, only a single image-driven registration step is required, unlike in conventional SPIM, where eight rotations and as many registration steps are needed. The resulting image (Fig. 2e) demonstrates sufficiently high quality that membrane segmentation was computationally straightforward across the entire embryo surface (Fig. 2f) and cell shape changes could be tracked over time (see Supplementary Note 6, Supplementary Fig. 9 and Supplementary Videos 10-12). Importantly, even during rapid morphological changes, such as ventral furrow formation, cell membranes could be fused and segmented at each time point (Fig. 2f).

In summary, MuVi-SPIM can record, without rotation, four inherently registered three-dimensional images of a specimen, and fuse them into a single high-quality image in real time. It enables rapid *in toto* imaging with sub-cellular resolution and allows investigation of highly dynamic biological processes in the context of the entire specimen. It also facilitates efficient and robust image processing. It is important to note that even when rotation is beneficial, e.g. to image cell shapes or improve resolution, MuVi-SPIM still represents a significant improvement over previous imaging methods for full embryo reconstruction. Here we used single photon illumination to demonstrate the advantages of the MuVi-SPIM configuration. The same arguments should also apply in case of different plane illumination schemes, such as non-scanned light-sheets[6], Bessel beams or two-photon fluorescence excitation[10,19]. MuVi-SPIM's reliability and speed will make it an important imaging tool to address fundamental questions on the interface between cell and developmental biology.

Methods

Methods are available online.

Acknowledgements

We thank the mechanical and electronics workshop of the European Molecular Biology Laboratory for customized hardware, Daniela Holzer, Tatjana Schneidt, and Hilary Gustafson for help with the flies and Gerrit Heuvelman and Malte Wachsmuth for discussion on optics. We thank Stefano DeRenzis and the Wieschaus lab for the Gap43-mCherry flies and Edward Lemke for hardware support. We thank Jan Ellenberg for helpful comments on the manuscript and anonymous reviewers for constructive comments. The advanced light microscopy facility of EMBL is acknowledged for kind support. We are grateful for financial support from EMBL, EIPOD and BIOMS.

Figure legends

Figure 1:
MuVi-SPIM microscope setup and data processing pipeline.

(**a**) MuVi-SPIM consists of two illumination and two detection arms arranged along two perpendicular axes.

(**b**) Specimen is held in a water-filled experimental chamber at the intersection of the illumination and detection axes.

(**c-d**) The specimen is mounted in a block of agarose and illuminated with a light-sheet from either of the illumination arms (light-sheet 1 and 2), while the fluorescence is recorded simultaneously by the two detection arms (camera 1 and 2).

(**e**) Four possible illumination/detection combinations (branches) produce four three-dimensional multi-view images. As the geometric relations between the images are determined *a priori*, four multi-view images are rapidly transformed into the same coordinate system and synthesized into a high-content fused image.

Figure 2:

MuVi-SPIM is capable of rapid and reliable imaging of highly dynamic developmental processes.

(**a**) Three-dimensional representation of his2Av-mCherry expressing *Drosophila* in cycle 11. Colour corresponds to the depth of the nuclei in the image; red nuclei are closest and blue nuclei are the farthest (see the coloured axes in the bottom left corner).

(**b**) Total number of nuclei in every cycle of syncytial blastoderm (note logarithmic scale). Time is with respect to the beginning of the imaging. Different colours correspond to different cleavage cycles and are used in the inset to indicate the mitotic front.

(**c**) Nuclei in the cycle 10, where different colours indicate different sister pairs. Not all pairs are coloured for clarity.

(**d**) Embryo from (c) after three further rounds of division.

(**e**) Three-dimensional reconstruction of a *Drosophila* embryo expressing the membrane marker gap43-mCherry in cycle 14. Alternating colours correspond to the image contributions from the eight different views. Inset shows a close-up view of the image fusion on the boundary between two different views.

(**f**) Modified equirectangular projection of the epidermal layer of an embryo during ventral furrow formation (see Supplementary Note 5). The ventral axis corresponds to the central cross-section. Neighbour dashed lines are separated by 50 μm on the surface of the embryo. Green/purple shading is same as in (e). Insets show segmentation (shown in red) of a subsection (denoted by red box) during ventral furrow formation. Green dots mark the positions of cell vertices. The denoted times correspond to the time after the first segmented image (which is 10 min earlier than the data shown in the main image).

Methods

1. Optical setup

Selective Plane Illumination Microscope (SPIM) is a fluorescence microscope, where a fluorescent specimen is illuminated from the side with a thin light-sheet (Supplementary Fig. 1), while the emitted fluorescence is imaged by an objective lens, which is perpendicular to the light-sheet. Multi-view SPIM (MuVi-SPIM) consists of four optical trains or "arms", arranged along two horizontal axes that intersect under right angle (Fig. 1a). Each of the four arms ends with a microscope objective lens that is focused onto a specimen, which lies in the intersection of the two microscope axes. Two collinear arms are used to illuminate the specimen and are therefore called illumination arms. Two arms on the axis perpendicular to the former are used to collect the fluorescence generated in the light sheet and record two images with two image sensors. They are referred to as detection arms.

MuVi-SPIM implementation creates a virtual light-sheet by scanning a laser beam through the field of view of the detection lens (a method sometimes referred to as digital scanned laser beam light-sheet microscope or DSLM), but different methods could also be used in MuVi-SPIM, e.g. a static light-sheet[6] or a scanning Bessel beam[19]. An illumination arm consists of a galvanometric scanner (VM500+, Cambridge Technology Inc.), scan lens (S4LFT0061/065, Sill optics GmbH and Co. KG), tube lens (TI-E 1x, Nikon Instruments Inc.) and objective lens (CFI Plan Fluor 10x/0.30W, Nikon Instruments Inc.). Each illumination arm is supplied with an illumination laser beam. A set of lasers with different wavelengths (Calypso 491 nm, Samba 532 nm, Jive 561 nm, Mambo 594 nm, all from Cobolt AB) is coupled into a single beam using a set of dichroic beam splitters (LaserMUX, Semrock Inc.), fed through an acousto-optical tunable filter (AOTFnC-400.650, A-A Optoelectronic) that controls the illumination intensity and wavelength, and coupled into an optical fiber (kineFLEX, Qioptiq Inc.) that transports the light to the microscope. There, the beam is collimated (0.7 mm beam diameter) and then diverted into the desired illumination arm using a motorized flip mirror (KSHM 40, Owis GmbH).

Each detection arm resembles a standard epifluorescence microscope and consists of an objective lens (CFI Apo 40x/0.80W or Apo LWD 25x/1.1w, both from Nikon Instruments Inc.), filter wheel (FW-1000, Applied Scientific Instrumentation) with a set of emission filters (LPD01-488RS-25 and BLP01-594R-25, both from Semrock Inc. and HQ525/30, Chroma Technology Corp.), tube lens (NT47-740, Edmund optics Inc.) and sCMOS camera (Neo, Andor Technology plc.). A 160 mm achromatic converging lens is used as a tube lens, which results in 32-times effective magnification. At this magnification, the image of a typical *Drosophila* embryo optimally covers the sCMOS image sensor.

Water dipping objective lenses used in the four arms require the specimen to be immersed in an aqueous medium. This is made possible by a special experimental chamber featuring four flexible nitrile-rubber membrane seals (Supplementary Fig. 2a). The chamber can thus be filled with a liquid, while the objective lenses and the chamber remain mechanically uncoupled. This is crucial for precise positioning of the objective lens and long-term stability of the microscope. Unlike in previous SPIM implementations, the specimen is held in the chamber from below using an original two-stage flexible seal. The latter consists of a Teflon ring seal, which permits specimen rotation, and of a flexible rubber tube, which allows translation of the specimen relative to the chamber. Coarse specimen translation is done using a manual two-axis linear stage (M-401 with two SM-13 Vernier micrometers, everything from Newport Corp.) and motorized vertical stage (M-501, Physik

Instrumente GmbH & Co. KG), while fine positioning is done by a two-axis piezo stage (P-628.2CL, Physik Instrumente GmbH & Co. KG). The latter is also used to move the specimen through the light-sheet to produce the three-dimensional images of the specimen.

To produce focused images, the light-sheet must illuminate only a thin section of the sample in the vicinity of the detection objective's focal plane. In MuVi-SPIM, the two light-sheets produced by the two illumination arms are aligned with each other using two galvanometric scanners, such that they illuminate exactly the same section. The waist of the light-sheet (i.e. the location along the light-sheet where it is the thinnest) is positioned near the intersection of the illumination and detection axes by axially translating the two illumination objectives using two Z-positioners (G061063000, Qioptiq). The two detection objective lenses are then focused onto the illuminated volume using another set of Z-positioners (same as above). One of the detection objective lenses also allows for precise lateral translation along the two directions perpendicular to its optical axis (XY-stage KT 65, Owis GmbH), in order to make both detection arms image precisely coincident rectangles. Lateral positioning of the illumination objective lenses is not necessary since their magnification is lower from that of the detection illumination lenses. Precise positioning of the light-sheets within the field of view of the illumination objective and their lateral size is adjusted using the galvanometric scanners.

2. Image fusion

Each of the four possible combinations of an illumination and a detection arm, referred to as imaging branches, generates a three-dimensional image. Four images are normally fused into a single high quality image, Supplementary Fig. 4. Geometric relations between the four images (i.e. functions that relate every pixel in one image with corresponding pixels in the remaining three images) are obtained using a diagnostic specimen (see Supplementary Protocol 2). A multi-view set of four images of the bead dispersion is acquired through the four imaging branches. Images of the bead dispersion are segmented, producing four lists of three-dimensional vectors that correspond to the locations of the beads as imaged through each of the four branches. Affine transformation parameters that optimally map each of the vector lists onto a chosen reference list is than obtained as described in Supplementary Note 4.

Since the geometric relations between the four views are defined solely by the optical arms (unlike in traditional SPIM implementations, where specimen must be rotated), the transformation parameters stay the same after the diagnostic specimen is replaced with any other fluorescent specimen. Image registration thus becomes a matter of applying the affine transformations to the images. Transformation of one 500 megapixel three-dimensional image on a 16-core PC thus takes approximately three seconds. MuVi-SPIM therefore produces virtually registered multi-view image sets in real-time. Unlike in previous multi-view SPIM implementations, quality of the MuVI-SPIM image registration does not depend on the content of the images. The microscope performs identically well with specimens that produce images with low intensity or contrast.

Registered images are then synthesized into a single high-quality image. This image is calculated as a locally weighted average of the four registered views; views that are expected to yield best image quality in a given part of the specimen are given locally highest weight.

In case of the *Drosophila* embryo the weights were calculated as follows. In the first image, outer shell of the embryo's body was detected. In every view, total path l of the excitation and emission light through the embryo's body was calculated for every pixel in the three-dimensional image. Weights were then calculated as $e^{-\eta l}$, where η defines the length of the transition between the images ($\eta = 50/\mathrm{pixel}$ gives good results and was used to generate Fig. 2a, Supplementary Videos 1-4). In effect, the final image is a mosaic of the four input views with sigmoid-like transition between them (Supplementary Fig. 4).

When fluorescent samples are imaged that require rotation (due to the limits of the point-spread-function), such as a membrane-marker expressing fly, the image alignment and fusion is more complex. As described in the main text, sample rotation by 90^{o} is required to image the entire embryo in sufficient detail, Supplementary Fig. 5. Beads are recorded for each view (0^{o} and 90^{o} rotation) and the four stacks from each viewpoint are aligned and fused as described above (so we now have two stacks). However, to fuse these two stacks into one final three-dimensional image requires image-based registration, since the transformations that bind the rotated views are strongly affected by microscopic drift of the specimen relative to the piezo stage and can therefore not be assumed constant[15]. We emphasize that MuVi-SPIM, in this situation, only requires two stacks to be registered using a data-driven algorithm (compared to eight in previous methods), and that due to the high information content of the two images being registered (each is already a fusion of four images), the image registration is reliable and eight times as fast as conventional multi-view SPIM.

The fused image is then calculated as a weighted average of the eight registered views. *Drosophila* embryo's long axis was detected in the first image and the volume of the embryo was split into eight cylindrical sectors, arranged symmetrically around the embryo axis. The eight sectors of the final image were then assembled, each originating from a different view (Supplementray Fig. 5a). Again, transition between two neighbouring sectors is softened by weights that resemble a sigmoid function. As only that sector of each view is retained, where the axis of detection arm intersects with the embryo surface under an angle equal or greater than 45^{0}, tangential resolution in the fused images is everywhere sufficient to resolve neighbouring cells, Supplementray Fig. 5b. Further details are in the Supplementary Notes 4-6.

Bead analysis and image synthesis were coded in Matlab (Mathworks Inc.) and the image affine transformation in C++ (Microsoft Visual Studio 2008, Microsoft Corp.) using Insight Toolkit libraries (http://www.itk.org). Image processing was done on a PC featuring two quad-core 2.4 GHz Intel Xeon CPUs and 48 GB of RAM.

3. Image analysis of nuclei dynamics in early *Drosophila* embryo

First we corrected for distortion of the fluorescence distribution due to the point spread function (PSF) of the microscope, using an approximation of the PSF[20] and a parallelized maximum likelihood deconvolution algorithm[21,22]. The resulting images were then background corrected using a top hat filter - results of which are shown in Supplementary Fig. 6a and Supplementary Video 1 - and filtered by a Mexican hat filter, with width corresponding roughly to the radius of an average nucleus[23].

To obtain the lineage of individual nuclei, the track over time of each nucleus has to be reconstructed. Snapshots of the fluorescence distribution of the nuclei where taken at fixed time

steps, resulting in a discrete spatio-temporal grid of fluorescence distributions. The data analysis was split into two steps: automatic segmentation of the nuclei from the fluorescence distribution separately for each time point and subsequent track reconstruction based on the centroids of the identified objects.

To segment the data, local thresholding yielded a segmentation of candidate objects, which were then kept or discarded, based on a volume criterion. Objects with volume greater than mean volume plus its standard deviation were split into separate objects using a watershed algorithm[24]. Supplementary Fig. 6b and Supplementary Videos 5-7 demonstrate the segmentation of the nuclei found using the above routine.

Once the centroids where obtained, the track reconstruction was reduced to a point-matching problem between consecutive times t and $t + \Delta t$. For two consecutive timepoints, a centroid pair consists of one member from each of the two time points representing the displacement of a nucleus. Due to high imaging rate, the displacement of nuclei between subsequent time points at the chosen temporal resolution did not exceed half the average neighbour distance (see Supplementary Video 5 and Supplementary Fig. 6d). Therefore, the tracks could be constructed based on nearest neighbour point matching. See Supplementary Note for further details.

4. Membrane analysis

To image the membrane marker around the entire embryo we used rotation to ensure that sufficient resolution tangentially to the embryo surface was achieved in all parts of the embryo. For the initial orientation we imaged as described above for the histone-mCherry expressing embryos (using 594 nm laser for excitation and RE594 emission filter), with 2 µm spacing along the z-axis and 41ms exposure time per z-position. The specimen was then rotated by 90^{o} and imaged again. In effect, for each imaging sequence eight three-dimensional images were taken. The total time between subsequent images was 51 seconds (43 seconds for the four stacks plus the time taken to rotate back to the initial position and reset the light-sheet flip mirror). For each time point the four image stacks were fused using methods discussed above. In Supplementary Videos 10 and 12, we demonstrate a full reconstruction of the embryo during cycle 14.

Images were analyzed using custom-written code in Matlab (Mathworks Inc.). During the time window of imaging, the majority of cells lie on the embryo periphery. Therefore, to analyze cell changes we “unrolled” the embryo using a modified equirectangular projection (Supplementary Note 5).

To analyze the unrolled data set, first background was removed from the data using morphological opening with a disk size of 25 pixel diameter and then a median filter (size 3 x 3) smoothed the data (note that analysis using unsmoothed data was almost identical). To segment the membranes we took advantage of the Matlab function *watershed.* Segmentation was generally accurate at all time points (> 95% cells correctly segmented), though during ventral and cephalic furrow formation the segmentation became less reliable and a limited amount of manual correction was required. Manual correction consisted only of adjusting the initial estimate of cell position for the *watershed* function and not the output (i.e. given a sufficiently good initial estimate of cell position, the data was of high enough quality to reliably segment). The Matlab function *bwmorph* was used on the segmented data to detect the cell vertices. In Supplementary Figure 9a-b we demonstrate segmentation of almost an

entire embryo in cycle 14 (pole regions are excluded). We find 4,889 cells, which is consistent with the expected number of cells at this stage.

5. Tracking of individual nuclei in ventral ectoderm

A *Drosophila melanogaster* embryo (His2Av-mCherry) was imaged (200 sections spaced by 1 µm) from early cycle 14 for 15 hours (at 30 second intervals) and then imaged every 10 minutes for a further 5 hours (imaging time for complete set of four views was 10 seconds) using a MuVi-SPIM with a pair of Nikon Apo LWD 25x/1.1w detection objective lenses. After fusion (as described above) images were filtered with a Mexican hat filter. Selected nuclei, which would become part of the ventral ectoderm, were tracked through several hours of development with a particle image velocimetry based tracking algorithm[25].

References

1. Wolpert, L. *et al. Principles of Development*. (Oxford University Press: 2006).
2. Lander, A. D. Pattern, Growth, and Control. *Cell* **144**, 955–969 (2011).
3. Lecuit, T. *Tissue Remodeling and Epithelial Morphogenesis (Current Topics in Developmental Biology): 89*. (Academic Pr Inc: 2009).
4. Siedentopf, H. & Zsigmondy, R. Uber Sichtbarmachung und Größenbestimmung ultramikoskopischer Teilchen, mit besonderer Anwendung auf Goldrubingläser. *Ann. Phys.* **315**, 1–39 (1902).
5. Voie, A. H., Burns, D. H. & Spelman, F. A. Orthogonal-plane fluorescence optical sectioning: three-dimensional imaging of macroscopic biological specimens. *J Microsc* **170**, 229–36 (1993).
6. Huisken, J., Swoger, J., Del Bene, F., Wittbrodt, J. & Stelzer, E. H. K. Optical Sectioning Deep Inside Live Embryos by Selective Plane Illumination Microscopy. *Science* **305**, 1007–1009 (2004).
7. Dodt, H.-U. *et al.* Ultramicroscopy: three-dimensional visualization of neuronal networks in the whole mouse brain. *Nat Meth* **4**, 331–336 (2007).
8. Keller, P. J., Schmidt, A. D., Wittbrodt, J. & Stelzer, E. H. K. Reconstruction of Zebrafish Early Embryonic Development by Scanned Light Sheet Microscopy. *Science* **322**, 1065–1069 (2008).
9. Keller, P. J. *et al.* Fast, high-contrast imaging of animal development with scanned light sheet-based structured-illumination microscopy. *Nat Meth* **7**, 637–642 (2010).
10. Truong, T. V., Supatto, W., Koos, D. S., Choi, J. M. & Fraser, S. E. Deep and fast live imaging with two-photon scanned light-sheet microscopy. *Nat Meth* **8**, 757–760 (2011).
11. Capoulade, J., Wachsmuth, M., Hufnagel, L. & Knop, M. Quantitative fluorescence imaging of protein diffusion and interaction in living cells. *Nat Biotech* **29**, 835–839 (2011).
12. Cella Zanacchi, F. *et al.* Live-cell 3D super-resolution imaging in thick biological samples. *Nat Meth* **8**, 1047–1049 (2011).
13. Swoger, J., Verveer, P., Greger, K., Huisken, J. & Stelzer, E. H. K. Multi-view image fusion improves resolution in three-dimensional microscopy. *Opt. Express* **15**, 8029–8042 (2007).
14. Preibisch, S., Saalfeld, S., Schindelin, J. & Tomancak, P. Software for bead-based registration of selective plane illumination microscopy data. *Nat Meth* **7**, 418–419 (2010).
15. Krzic, U. Multiple-view microscopy with light-sheet based fluorescence microscope. PhD Thesis, University of Heidelberg (2009)
16. Huisken, J. & Stainier, D. Y. R. Even fluorescence excitation by multidirectional selective plane illumination microscopy (mSPIM). *Opt. Lett.* **32**, 2608–2610 (2007).
17. Foe, V. E. & Alberts, B. M. Studies of nuclear and cytoplasmic behaviour during the five mitotic cycles that precede gastrulation in Drosophila embryogenesis. *Journal of Cell Science* **61**, 31–70 (1983).
18. Goshtasby, A. *2-D and 3-D image registration for medical, remote sensing, and industrial applications*. (John Wiley and Sons: 2005).
19. Planchon, T. A. *et al.* Rapid three-dimensional isotropic imaging of living cells using Bessel beam plane illumination. *Nat Meth* **8**, 417–423 (2011).
20. Grill, S. & Stelzer, E. H. K. Method to calculate lateral and axial gain factors of optical setups with a large solid angle. *J. Opt. Soc. Am. A* **16**, 2658–2665 (1999).
21. Quammen, C. W., Feng, D. & Taylor II, R. M. Performance of 3D Deconvolution Algorithms on Multi-Core and Many-Core Architectures. *University of North Carolina at Chapel Hill, Department of Computer Science, Tech. Rep* (2009).
22. Richardson, W. H. Bayesian-Based Iterative Method of Image Restoration. *J. Opt. Soc. Am.* **62**, 55–59 (1972).
23. Gonzalez, R. C., Woods, R. E. & Eddins, S. L. *Digital image processing using MATLAB*. (Prentice Hall: 2003).
24. Meyer, F. Topographic distance and watershed lines. *Signal processing* **38**, 113–125 (1994).
25. Raffel, M., Willert, C. E. & Kompenhans, J. *Particle image velocimetry: a practical guide*. (Springer: Berlin; New York, 1998).

List of supplementary items

Supplementary File	Title
Supplementary Figure 1	Principle of a Selective Plane Illumination Microscope (SPIM)
Supplementary Figure 2	MuVi-SPIM experimental chamber
Supplementary Figure 3	Quantification of the relative drift of the MuVi-SPIM views
Supplementary Figure 4	MuVi-SPIM image synthesis
Supplementary Figure 5	MuVi-SPIM image synthesis in case of specimen rotation
Supplementary Figure 6	Cell tracing in early Drosophila embryo
Supplementary Figure 7	Cell tracking in the Drosophila ventral ectoderm
Supplementary Figure 8	Effects of anisotropic point-spread function on the imaging of cell membranes in Drosophila embryo
Supplementary Figure 9	Detailed view of the gap43-mCherry Drosophila embryo surface
Supplementary Figure 10	Light-sheet alignment using a fluorescent medium
Supplementary Note 1	Light-sheet properties
Supplementary Note 2	Microscope instrument control architecture
Supplementary Note 3	Assessment of imaging time
Supplementary Note 4	Calculation of transformation parameters
Supplementary Note 5	Equirectangular projection of Drosophila embryo's surface
Supplementary Note 6	Further details on analysis of Drosophila embryo images
Supplementary Protocol 1	Light-sheet alignment
Supplementary Protocol 2	Diagnostic specimen preparation
Supplementary Protocol 3	Drosophila embryo preparation and mounting
Supplementary Video 1	Rotation of a background corrected raw His2Av-mCherry tagged embryo in cycle 11. Colour codes for depth (blue-labelled nuclei are on one side, red-labelled nuclei are on the other side).
Supplementary Video 2	Fused raw data of an embryo expressing His2Av-mCherry for a single time point in cycle 13. Depth inside the embryo is indicated left. Adjacent images in the three-dimensional stack were taken 2 µm apart from each other. Anterior (A) - posterior (P) and dorsal (D) - ventral (V) axes of the embryo are indicated in the top-right corner.
Supplementary Video 3	A view on the raw data from the Supplementary Movie 2 along the embryo's long axis**,** shown from the anterior to the posterior pole. Slice spacing is 0.5µm. The dorsal (D) - ventral (V) axis is indicated.
Supplementary Video 4	Anaglyphic three-dimensional representation of the image from the Supplementary Movie 2. The image was background corrected and processed for red-cyan anaglyph glasses.
Supplementary Video 5	Dynamics of nuclear motion. Positions of the segmented nuclei are shown at time T (indicated in top right corner) and 10 preceding time points. Colour ranges from blue to yellow, where the former corresponds to the time T, and the latter to T – 250 seconds.
Supplementary Video 6	Tracking of nuclei. Each point represents a tracked nucleus. After division, one of the daughter nuclei is assigned the mother's colour and the other nucleus is assigned a new unique colour. Scale bar corresponds to 70 µm.
Supplementary Video 7	Velocity of nuclei. Each point represents a nucleus. Its position

	is shown for the current and previous four time points. The colour indicates velocity of each nucleus (see colour bar at the bottom). Scale bar corresponds to 70 μm.
Supplementary Video 8	Ventral and the dorsal (inset) views of a Drosophila embryo starting from early cycle 14. The embryo was imaged for 15 hours every 30 seconds, and for a further 5 hours every 10 minutes to confirm that the high frame-rate imaging didn't alter the embryonic development. Only one image every 10 minutes is shown in the movie after the initial 5 hours. Every three dimensional image was background corrected and maximum-projected from a middle plane towards ventral and dorsal side respectively using Fiji (www.fiji.sc).
Supplementary Video 9	Six nuclei, which become part of the ventral ectoderm from the recording shown in Supplementary Video 8, were tracked through several hours of embryogenesis. The left panel shows tracked colour-coded nuclei (parent and daughter nuclei have same colour) with path traces. Right panel shows a magnified region around the five leftmost nuclei. Each coloured dot marks the brightest pixel of the appropriate nucleus. Note that this movie is a two-dimensional projection of the data but the trajectories are tracked in three-dimensions. Hence, sometimes nuclei appear to intersect but in three-dimensions the nuclei move past each other without collision.
Supplementary Video 10	Rotating *Drosophila melanogaster* embryo expressing gap43-mCherry membrane marker in cycle 14, corresponding to Fig. 2e.
Supplementary Video 11	Four concurrently running perpendicular sections through a gap43-mCherry membrane marker expressing embryo during cycle 14. Top panels are the opposing lateral views, bottom left is ventral view and bottom right is dorsal view. This movie corresponds to Supplementary Fig. 9c.
Supplementary Video 12	View along the long-axis of a *Drosophila melanogaster* embryo expressing gap43-mCherry membrane marker at a fixed time point, 10 minutes prior to ventral furrow formation.

Figure 1

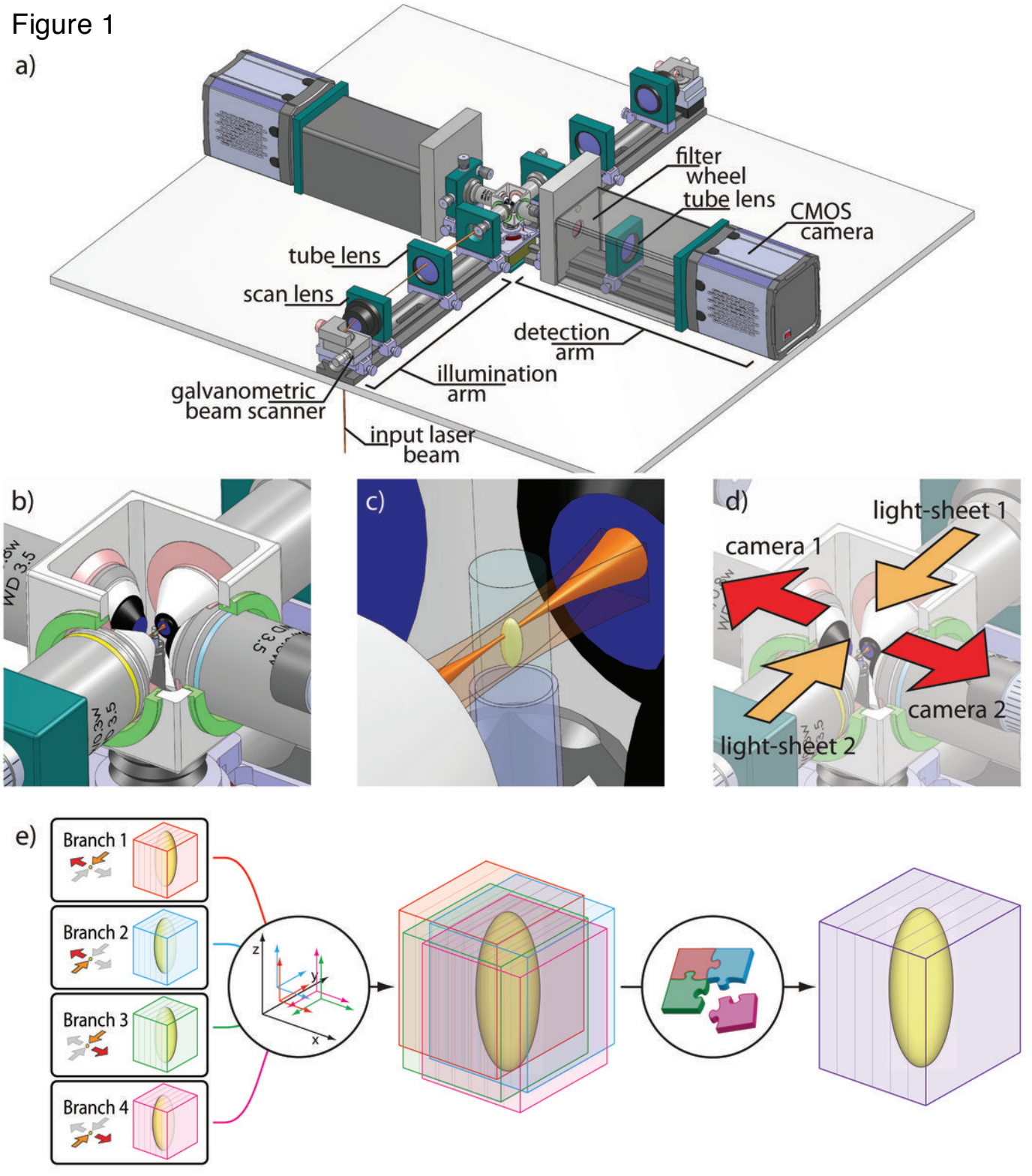
a)
filter wheel
tube lens
CMOS camera
tube lens
scan lens
detection arm
illumination arm
galvanometric beam scanner
input laser beam
b)
c)
d)
light-sheet 1
camera 1
camera 2
light-sheet 2
e)
Branch 1
Branch 2
Branch 3
Branch 4
z
y
x

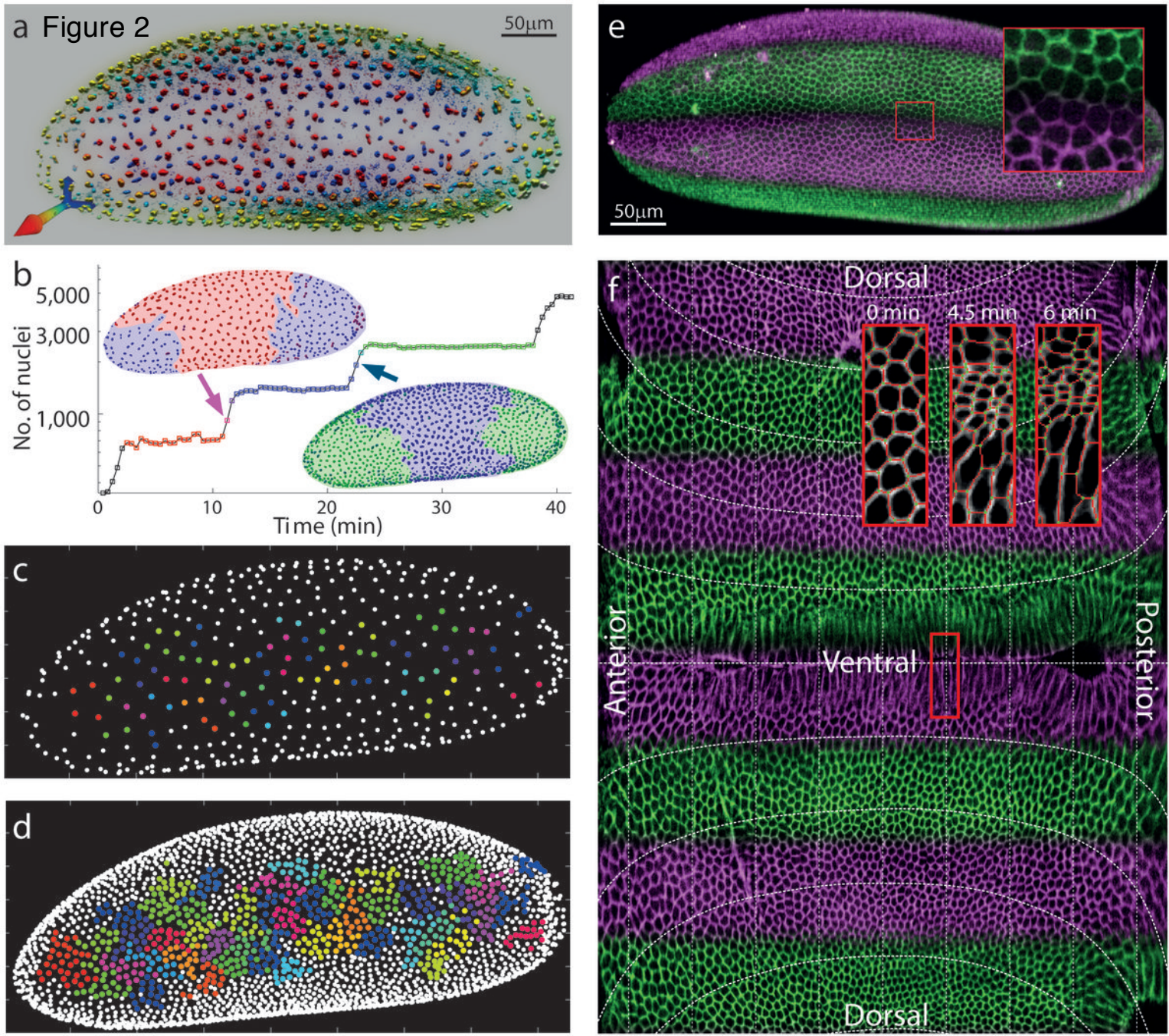
a Figure 2
50μm
b
5,000
3,000
1,000
No. of nuclei
0
10
20
30
40
Time (min)
c
d
e
50μm
f
Dorsal
0 min
4.5 min
6 min
Anterior
Posterior
Ventral
Dorsal

Multi-view light-sheet microscope for rapid *in toto* imaging

Uros Krzic[1], Stefan Gunther[1,2], Timothy E Saunders[1,2], Sebastian J Streichan[1], and Lars Hufnagel[1]

[1]Cell Biology and Biophysics Unit, [2]Genome Biology Unit
European Molecular Biology Laboratory, Meyerhofstr. 1, D-69117 Heidelberg, Germany

Note: Supplementary Videos are available on the Nature Methods website.

Supplementary Figure 1

Principle of a Selective Plane Illumination Microscope (SPIM). A fluorescent specimen (a *Drosophila melanogaster* embryo) is illuminated with a thin light sheet, while the emitted fluorescence is collected by an objective lens, which is oriented normally to the illumination objective lens. A thin section of the specimen is thus imaged. By taking a series of recordings while the specimen is moved along the detection objective's axis (blue arrow), a three-dimensional image is acquired.

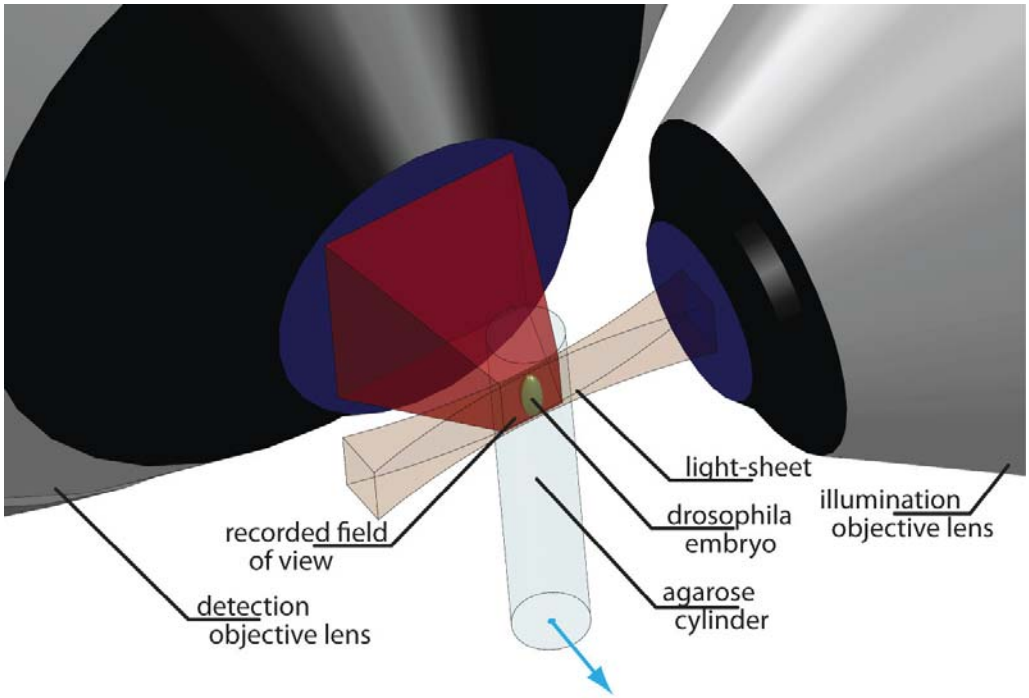

Supplementary Figure 2

MuVi-SPIM experimental chamber. **(a)** Four thin nitrile-rubber membrane seals allow the chamber to be filled with an aqueous medium, while the four objective lenses (one is not shown) and the chamber remain mechanically uncoupled. Specimen, which is held from below, can be moved relative to the chamber due to a flexible rubber tube that connects the XY-stage and the chamber. Rotation of the specimen relative to the chamber is made possible by a Teflon ring seal. As the ring is fixed in respect to the rotary and translation stages, rotation results in no additional tension on the rubber tube and does not tilt the specimen holder. **(b)** A mounted *Drosophila melanogaster* embryo. A cylindrical block of agarose gel holds the embryo, while the gel is held by a glass micropipette capillary. The embryo is approximately 500 µm long.

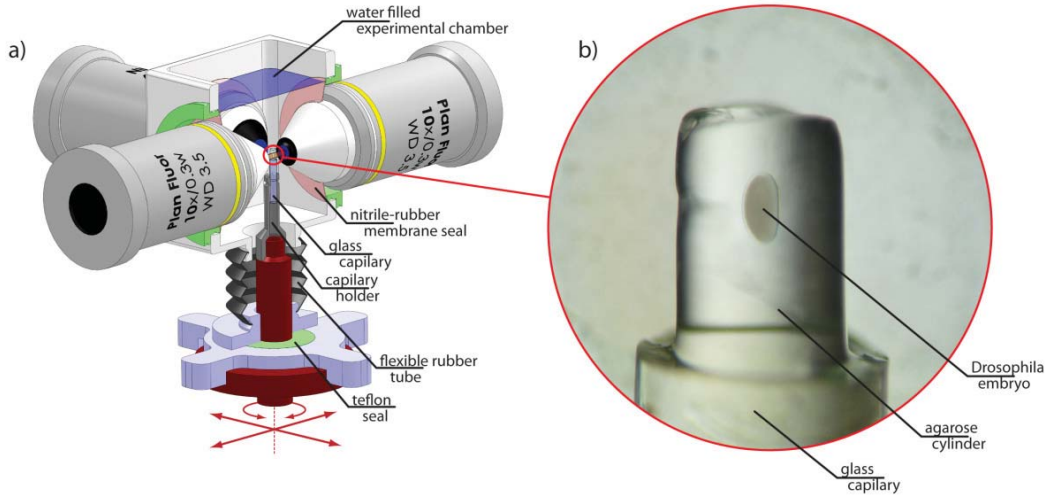

Supplementary Figure 3

Quantification of the relative drift of the MuVi-SPIM views. *Drosophila* embryo sized volumes of fluorescent beads were imaged 16 times, once every hour with both light sheets and cameras. Affine transformation parameters between the four stacks were determined for each time point as described in Supplementary Note 4. Fluctuations in the affine coefficients from one time point to another reflect relative dislocation of an image produced by a given imaging branch relative to the reference branch. Plot shows maximum displacements across the entire 3D volume for one of the three non-reference views (other two produce comparable results). Displacement is typically very low (less than 100 nm) in the centre of the imaged volume and increases linearly with the distance from the centre. Values displayed in the plot are reached only in the corners of the imaged volume. In most of the three-dimensional image, the displacement between the views is smaller than the optical resolution of the microscope even after many hours.

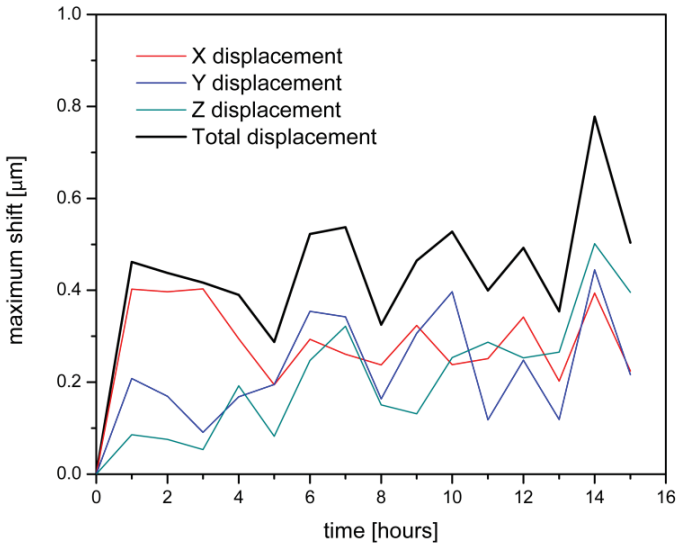

Supplementary Figure 4

MuVi-SPIM image synthesis. **(a)** Volume of the *Drosophila* embryo is split into four sectors, arranged symmetrically around the embryo's long axis. **(b)** Images show a section through the embryo perpendicular to the anterior-posterior axis, around 130 µm from the anterior end. In the centre is the image fused from the four images in the corners. The image is synthesized such that each of the four MuVi-SPIM views contributes one segment (divided by the dotted lines), where its local image quality is best.

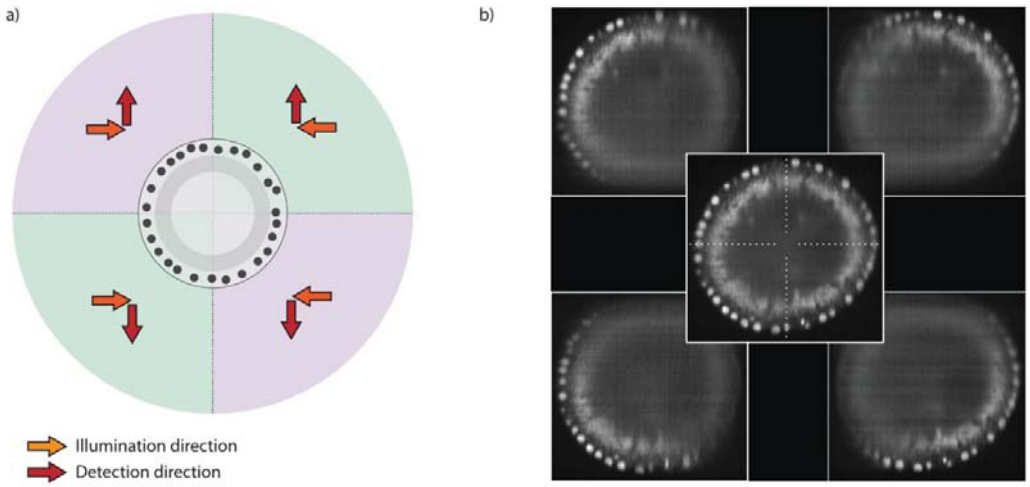

Supplementary Figure 5

MuVi-SPIM image synthesis in case of specimen rotation. **(a)** Volume of the *Drosophila* embryo is split into eight sectors, arranged symmetrically around the embryo's long axis. **(b)** Images show a section through the middle of the embryo perpendicular to the anterior-posterior axis. The middle image was synthesized from the multi-view images surrounding it. Each of the eight views contributes one sector to the final image, where the view's image resolution tangentially to the embryo surface and its local image quality are best.

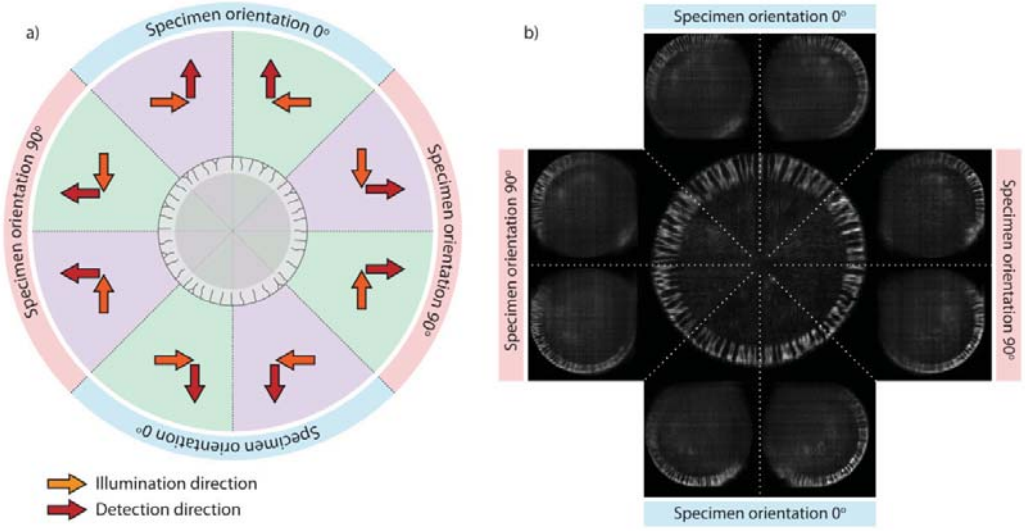

Supplementary Figure 6

Cell tracing in early *Drosophila* embryo. **(a)** Cell nuclei of embryo in cycle 11, 650 seconds after start of analysis. Colour codes for depth, ranging from close (blue) to far (red). Coloured coordinate axes in the lower left corner are a guide to the eye. Scale bar indicates 70 µm. **(b)** Embryo split into anterior half, where segmentation results are shown, and posterior part where original data is shown in grey scale. Colours in anterior part indicate depth as in (a). Coloured coordinate axes in the lower left corner are a guide to the eye. Tracks are shown throughout the embryo and colour coded for time as indicated by the coloured scale bar (bottom right) ranging from 150 s to 650 s. White scale bar indicates 70 µm. **(c)** Left panel: three-dimensional zoom on white square box in (a). Individual time points 600 s, 625 s, 650 s and 675 s are shown. Nuclei inherit their colours from their mother cells. Black spots indicate shadows of the nuclei. Scale bar is 30 µm. Right panel: close-up of the white rectangular box in (a). Individual time points 650 s, 675 s, 700 s and 725 s are shown, with selected nuclei coloured. Upon division, one of the daughter cells is assigned a new colour. Tracks are colour coded for time as indicated by the scale bar (bottom) ranging from 500 s to 725 s. **(d)** The shortest distance between any two nuclei as a function of time (black diamonds) and double maximum displacement during a time step (red squares). Mean distance is shown as black solid line with gray shade showing the standard deviation . **(e)** Median nuclear speed as a function of time. Red, blue and green colours correspond to mitotic cycles 11, 12 and 13, respectively. See Fig. 2b for comparison.

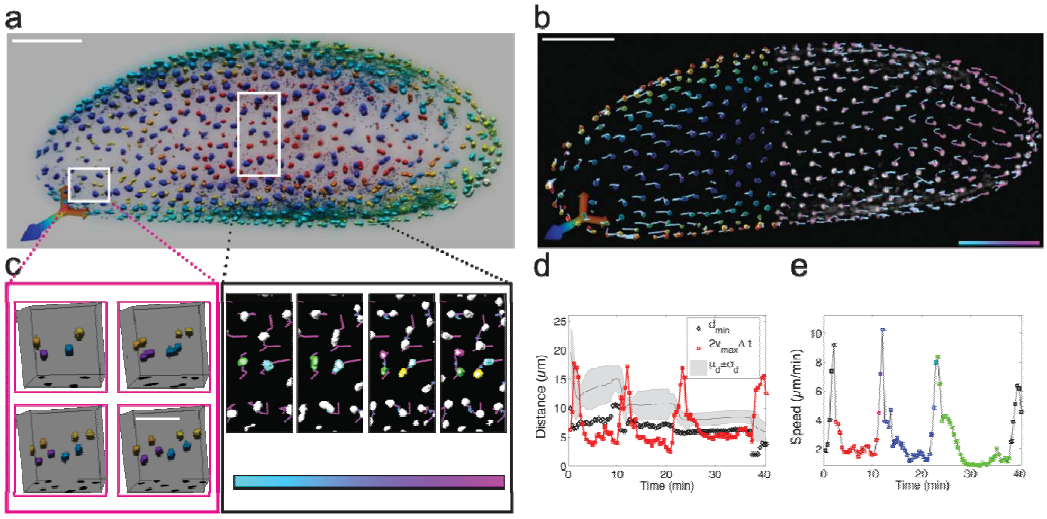

Supplementary Figure 7

Cell tracking in the *Drosophila* ventral ectoderm. Left column shows maximum intensity projections of the ventral side of a his2Av-mCherry *Drosophila* embryo at four different times (T = 0 h defined as start of imaging). Six nuclei are chosen for tracking (five grouped close together and one further apart) and followed through five hours of development. Daughter nuclei are labelled in the same colour as the parent nucleus. Middle column corresponds to the region highlighted by the white box in the left column. Traces of the nuclear trajectories are also shown in the same colour as the corresponding nucleus. The right column shows a close up view of the five closely grouped cells. Cell markers are centred on the position of maximum intensity for each cell.

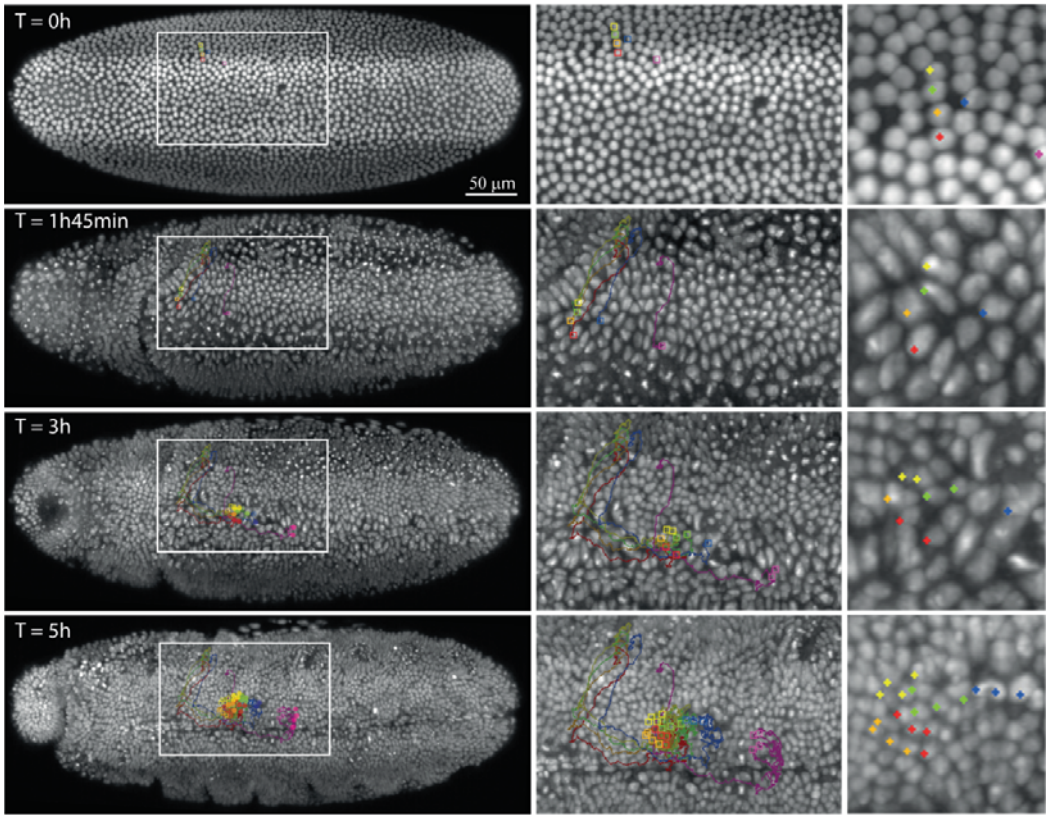

Supplementary Figure 8

Effects of anisotropic point-spread function on the imaging of cell membranes in *Drosophila* embryo. **(a)** Point-spread function (PSF) of the MuVi-SPIM is elongated along the microscope's detection axis. **(b)** In an early *Drosophila* embryo, most cells after cellularisation lie close to the embryo's surface; the membranes between the cells are thus nearly perpendicular to the embryo's surface. The illustration shows a cross-section through a *Drosophila* embryo perpendicular to the embryo's long axes. Left two columns show the orientation of the PSF relative to the embryo, with the embryo's angular position of 0^0 and 90^0, respectively. The fused image (right column) is constructed from the input images such that the membranes and the microscope's PSF are everywhere close to parallel. **(c)** Orientation of the microscope's PSF relative to the orientation of the fluorescent membranes determines image quality (embryo surface was "unrolled" as described in Supplementary note 5). In a single MuVi-SPIM image set without specimen rotation (left two columns), membranes will be best resolved where they are nearly parallel to the microscope's PSF, while in the areas where the membranes are nearly perpendicular to the PSF, image contrast and resolution are significantly reduced. In a fused image produced from two rotated MuVi-SPIM datasets (right column), the PSF is never perpendicular to the cell membranes; the resulting image contrast and resolution are therefore sufficient to resolve individual cells almost anywhere on the embryo's surface (See Supplementary Video 10).

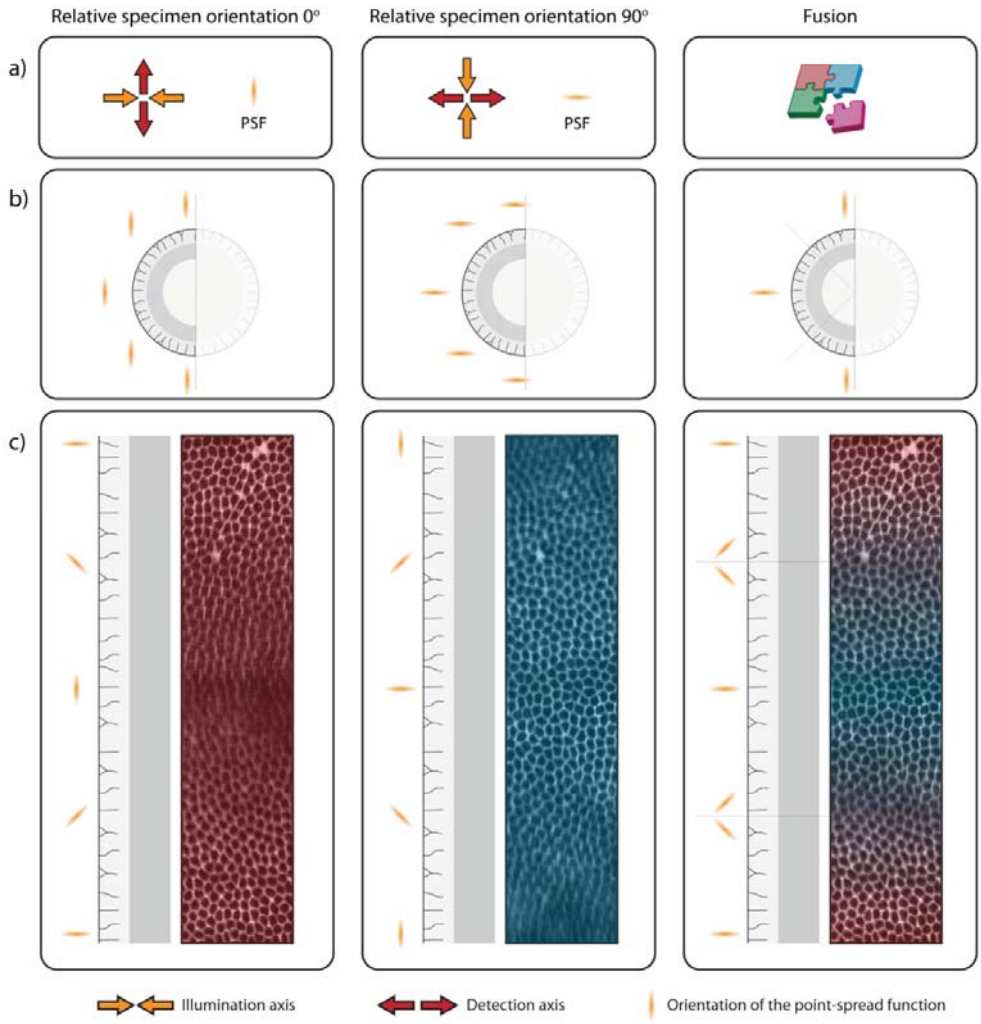

Supplementary Figure 9

Detailed view of the gap43-mCherry *Drosophila* embryo surface. **(a)** Segmentation of the membranes in an embryo during early cycle 14 (excluding polar regions). Greyscale data is the fused and unrolled image with red lines denoting segmented cell borders. **(b)** Close-up of the highlighted region in (a). **(c)** Time-lapse view of cell movements and shapes during early *Drosophila* morphogenesis. The left schematic describes the viewpoints (and color scheme) shown in right panels (i-xii). (i-xii) Colored dots correspond to cell centres as found from image segmentation. The subsequent time points show cells tracked cells for up to 20 minutes. **(d)** From the tracking data shown in (c), cell speeds can be calculated. Time is defined from the first image of the time-lapse (four minutes before onset of ventral furrow formation). Arrows labelled (1-3) denote times where different morphological events occur: the onset of ventral furrow formation (1), the onset of cephalic furrow formation (2) and the beginning of germband extension (3).

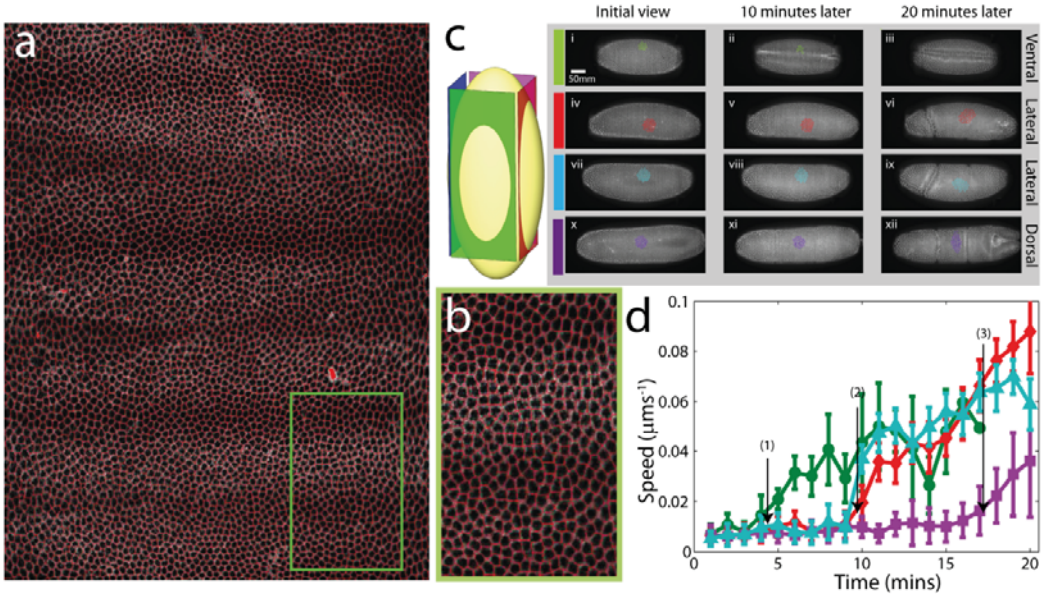

Supplementary Figure 10

Light-sheet alignment using a fluorescent medium. **(a)** When no emission filter is used in the detection arm, particles floating through the parked illumination beam generate circular shapes in the image. Size of the circles is roughly proportional to the distance of the particle (and therefore from the parked laser beam) from the focal plane of the detection arm. Large variation in the circles' sizes implies axial misalignment of the illumination objective lens, while uniformly sized circles (as is the case in the figure) point to axial misalignment of the detection objective lens. **(b-c)** Once an emission filter is inserted, fluorescence generated in the parked laser beam reveals precise position and shape of the beam's waist. Axially asymmetric beam implies axial misalignment of the illumination objective lens (b), while a symmetric but thick beam indicates axial misalignment of the detection lens (c). **(d)** In a well aligned SPIM, a parked laser beam generates an image of the beam with its waist near the centre of the image. Thickness of the waist is minimal, i.e. any axial movement of the detection objective lens will increase it. Properties of the light sheet (e.g. thickness and the Rayleigh range) can now be readily measured. For demonstration purposes, the beam waist in this figure is sub-optimally thin, which results in a high beam divergence and a light-sheet that is considerably thicker at the sides of the field of view than in the middle. **(e)** It is often useful to displace the both light-sheets, moving each waist for a fraction of the light-sheet's usable length in the direction opposite to the direction of light. This trick can up to double light-sheet's usable length without affecting its thickness. In this example, two light-sheets with usable lengths (defined as twice the Rayleigh range[1]) of 133μm are displaced for approximately 100μm, resulting in an effective light-sheet with thickness between 2.3μm and 3.2μm over the whole *Drosophila* embryo. **(f)** Once the SPIM is aligned, galvanometric scanner is used to scan the beam over the field of view, generating a homogeneous light-sheet. For demonstration purposes, scanning amplitude is set a bit below optimal in this figure, leaving parts of the image not illuminated.

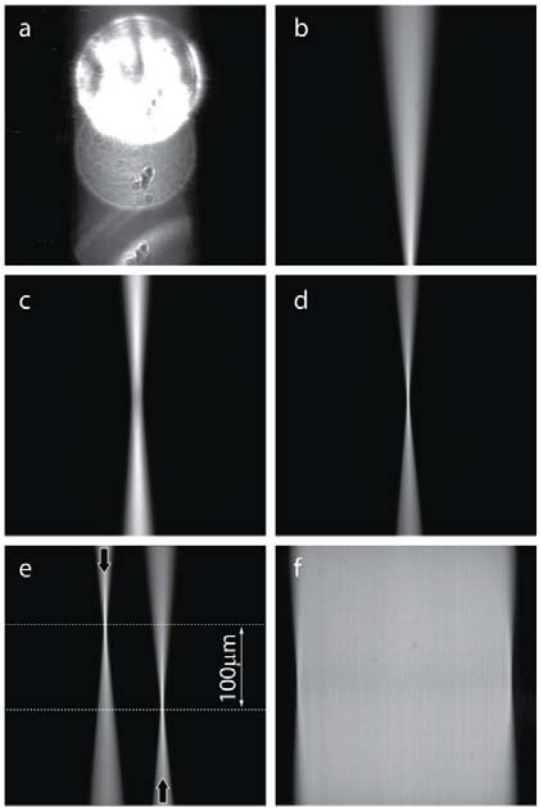

Supplementary Note 1

Light-sheet properties

Properties of the light-sheet can be easily obtained from the image generated by a well focused parked beam illuminating a fluorescent medium (see also Supplementary Protocol 1 and Supplementary Fig. 10d). In our case, the beam waist radius was measured to be $W_0 = 2.3\ \mu m$ (e^{-2} radius[1]), which corresponds to depth of focus (twice the Rayleigh range) of $2z_0 = 133\ \mu m$. After the waists of the both beams are displaced for roughly 100 μm (Supplementary Fig. 10e), effective light-sheet thickness is between 2.3 μm and 3.2 μm over the whole *Drosophila* embryo (around 200μm in diameter). Size of the light-sheet in the direction perpendicular to the illumination axis is defined by the scanning range of the galvanometric scanners and was set at around 550μm for imaging of *Drosophila* embryos (around 500 μm in length).

Lateral resolution (within the focal plane) of the microscope is determined by the numerical aperture of the detection objective lens and will be around 0.43 μm^2 in case of the 40x/0.8W lens and 610 nm emission (as used for *Drosophila* imaging). Axial resolution (along the detection axis) will be driven primarily by the axial resolution of the detection lens (2.28 μm with 40x/0.8W), although a minor improvement (around 10% at the waist of each light-sheet) is expected due to the light-sheet illumination[3].

Supplementary Note 2

Microscope instrument control architecture

The microscope control electronics is build around two high-speed analog output cards (NI PCI-6733 and PCIe-6259, National Instruments Corp.). Analog output channels are used to directly set the laser intensities (using an acousto-optical tunable filter, see Optical setup in Methods), positions of XY-Piezo stage and galvanometric scanners (through MiniSax Boards, Cambridge Technology Inc.). To ensure microsecond precise timing, voltage traces for these devices are pre-computed and then uploaded onto the cards together with corresponding digital traces to trigger camera, AOTF blanking and illumination steering flip-mirror. Filter wheel, specimen rotation and specimen vertical translation are controlled over RS232 ports, as their operation is not time critical.

An important part of MuVi-SPIM is the efficient and fast handling of the large amounts of data. The full image acquisition and processing pipeline comprises of four computers: a microscope control computer (Intel Core2Duo running at 3.16 GHz, 4 GB RAM); two camera computers (each featuring two quad-core 2.4GHz Intel Xeon CPUs, 24 GB of RAM and Areca ARC 1880I RAID controller with four 2 TB hard drives); and a data analysis computer (see Image fusion in Methods). An 80 TB RAID6 based storage system (using a 3Ware 9750-8i RAID controller) is used to store the large amounts of data produced by MuVi-SPIM. A private 10 gigabit Ethernet optical network allows for fast transfer of images between the microscope, storage system and image processing computer, and communication between the microscope computers.

The microscope is controlled by a custom-written program coded in LabView (National Instruments Corp.) that handles the communication with the electronics and the other computers.

Supplementary Note 3

Assessment of imaging time

All-around imaging with MuVi-SPIM is faster than with a regular SPIM[4] or mSPIM[5] for two distinct reasons. The first issue concerns the time the specimen is actually imaged (excluding the time required for rotation) at each time point. MuVi-SPIM produces virtually registered images, while rotation based multi-view imaging with SPIM or mSPIM requires image-based image registration. The latter necessitates sufficient overlap between the different views, which inevitably leads to some areas being imaged multiple times. The exact size of the necessary overlap depends on the properties of the specimen (specimen with low penetration depth and/or lacking sharp features will generally require larger overlap between the views). In theory, this overlap could be reduced to a fraction (as little as 20%) of the total specimen size, however as the effectiveness of the registration cannot be assessed until it is actually executed, low overlap puts results of the entire recording at risk. Moreover, since geometrical relations between the views are not known beforehand, it is difficult to ensure that every part of the specimen is covered by at least one view if the overlap is too low. In practice, to avoid the problems of insufficient overlap, the whole specimen is often chosen to be imaged after every rotation, effectively doubling (in mSPIM) or quadrupling (in regular SPIM) the time required for imaging.

Secondly, the speed with which a gel-held specimen can precisely rotate is limited. The rotary motor used in MuVi-SPIM, which is proven to meet multi-view microscopy requirements[4,6], requires 20 seconds for a full 360^0 rotation. This is also the additional time required for a single rotation-based multi-view acquisition using this motor; no matter how many views are taken, the specimen has to be rotated for 360^0 degrees in total to produce an all-around multi-view dataset when using a single detection arm. As rotation adds a fixed time to the total recording time, it will have an especially dramatic impact on the resulting frame rate if the imaging time (without rotation) is very short. For example, MuVi-SPIM routinely records a four-view dataset of a *Drosophila* embryo in less than 20 seconds (and could do it faster if required); adding another 20 seconds for rotation would therefore more than double the acquisition time.

Both issues together make MuVi-SPIM at least 2-4 times faster than mSPIM or SPIM, achieving time scales relevant for many biological processes. Concretely, *in toto Drosophila* embryogenesis was imaged in MuVi-SPIM at least 9 times faster than in previously published similar work[7] (20 seconds in MuVi-SPIM vs. 3 minutes in DSLM-SI), finally enabling reliable tracking of the nuclei. A faster rotation motor (provided that the specimen mounting allows it) might narrow the gap in speed. However the fact that no such fast rotation has been implemented in eight years since the idea of rotation-based multi-view imaging with SPIM was first put forward, might point to considerable technical difficulties in this approach.

Supplementary Note 4

Calculation of transformation parameters

Geometric relations between the four images (i.e. functions that relate every pixel in one image with corresponding pixels in the remaining three images) are obtained using a diagnostic specimen (see Supplementary Protocol 2). A multi-view set of four images of the bead dispersion is acquired through the four imaging branches. Images of the bead dispersion are segmented, producing four lists of three-dimensional vectors that correspond to the locations of the beads as imaged through each of the four branches.

One of the four views is chosen as a reference. Geometric relations between the remaining three views and the reference view are then searched in the space of three-dimensional affine transformations: Let's assume we are trying to find an affine transformation $\mathcal{M}$ that optimally maps a vector list L_2 onto a reference vector list L_1, where

$$L_1 = \left[\vec{r}_1^{\,1}, \vec{r}_2^{\,1}, \ldots\ \vec{r}_{N_1}^{\,1}\right],\ L_2 = \left[\vec{r}_1^{\,2}, \vec{r}_2^{\,2}, \ldots\ \vec{r}_{N_2}^{\,2}\right] \tag{1}$$

and

$$\mathcal{M}_{M,\vec{t}}(\vec{r}) = M \cdot \vec{r} + \vec{t}\,. \tag{2}$$

Here, M is a 3x3 matrix. Both vector lists represent the same distribution of fluorescent beads in the diagnostic specimen, but it is not known which vector $\vec{r}_n^{\,1}$ corresponds to which vector $\vec{r}_m^{\,2}$. Moreover, some beads were most probably detected in only one of the two images and lack a corresponding vector in the second set.

We define a merit function

$$f\left(M, \vec{t}\right) = \sum_{i=1}^{N_1}\sum_{j=1}^{N_2} \Theta\left(\left|\mathcal{M}_{M,\vec{t}}\left(\vec{r}_j^{\,2}\right) - \vec{r}_i^{\,1}\right|\right) \tag{3}$$

where $\Theta(\mathrm{d})$ can be any function that is finite at $\mathrm{d} = 0$ but drops close to 0 at $\mathrm{d} \gg \lambda$, for example $\Theta(\mathrm{d}) = \mathrm{e}^{-\lambda \mathrm{d}^2}$. Parameter λ should approximately equal the localization accuracy (typically around 100 nm) of the bead segmentation algorithm, but can be increased to enlarge merit function's basin of attraction at the expense of the global minimum's depth.

Function (3) is optimized using a downhill algorithm[8]. Our optimized version of the algorithm requires approximately 3 seconds to find a global minimum of the function (3) with a sub-pixel precision and $N_1 \approx N_2 \approx 1000$.

Supplementary Note 5

Equirectangular projection of Drosophila embryo surface

With a single 90° rotation there are eight views of the embryo, Supplementary Fig. 5. The eight views were fused into a single image using the method described in Methods. Next, defining z as the direction along the long-axis of the embryo, each z-plane was analyzed separately. The embryo in every two-dimensional image corresponding to each z-coordinate was approximated by a circle of radius $r(z)$ (the radius of the circle depends on the z-position) and a centre at $(x(z), y(z))$. The image was then transformed from Cartesian (x, y, z) coordinates into modified cylindrical coordinates (ϑ, ϱ, z') using the following relations:

$$\begin{aligned} x &= r(z')\,\varrho\,\cos\vartheta + x(z') \\ y &= r(z')\,\varrho\,\sin\vartheta + y(z') \\ z &= z' \end{aligned} \tag{4}$$

Here, radial coordinate is normalized by the radius of the embryo at a given z', such that $\varrho = 1$ defines the surface of the embryo. Finally, a maximum radial projection through the ϱ range that corresponds to the depth range of interest in the embryo ($\mathrm{P} = (0.85, 0.86)$ in Fig. 2) was calculated as follows:

$$I_p(z', \vartheta) = \max_{\varrho \in \mathrm{P}} I(\vartheta, \varrho, z') \tag{5}$$

In Fig. 2f, $I_p(z', \vartheta)$ is shown with z' along the horizontal axis and ϑ along vertical axis.

Supplementary Note 6

Further details on analysis of Drosophila embryo images

Early *Drosophila* development

Drosophila melanogaster embryogenesis takes place inside an egg with constant shape and volume. After fertilization and pronuclear fusion inside the yolk, mitotic nuclear divisions proceed in synchrony so that the nuclei number virtually doubles during each mitotic cycle. During the first 13 cycles nuclei divide in a syncytium, i.e. all nuclei share the same cytoplasm of the entire egg. After 9 rounds of divisions most of the nuclei migrate from the eggs interior towards the egg surface. The surface nuclei divide 4 more times with a rate up to 8 minutes per cycle and remain bound to the surface[9]. During each round of division waves of nuclear divisions can be observed[10]. These waves are fast compared to the duration of the division cycle and usually emanate from the embryo poles and meet in the mid-part of the embryo.

After the thirteenth round of division the nuclei begin to form cell walls. During this period membranes start to form and many of the embryos distinctive structures (e.g. the head) become defined. Processes such as ventral and cephalic furrow formation result in the internalization of many of the newly formed cells.

Extended discussion of nuclei analysis

We imaged *Drosophila* labelled by fluorescently-tagged histone proteins (His2Av-mCherry) using the 594 nm laser and 625/30 band pass emission filter, in order to track chromosomal spatial positions across nuclear division cycles in the early embryo. Images with fluorescence distribution of His2Av-mCherry obtained by fusion of four individual images, as described above, were sent though a sequential image-processing pipeline to obtain a segmentation of nuclei for each time point (Methods).

To obtain the lineage of individual nuclei, the tracks over time of each nucleus have to be reconstructed. Snapshots of the fluorescence distribution of the nuclei where taken at fixed time steps, resulting in a discrete spatio-temporal grid of fluorescence distributions. The data analysis was split into two steps, namely automatic segmentation of the nuclei from the fluorescence distribution separately for each time point and subsequent track reconstruction based on the centroids of the identified objects.

Once the centroids where obtained, the track reconstruction was reduced to a point-matching problem between consecutive times t and $t + \Delta t$. For two consecutive timepoints, a centroid pair consists of one member from each of the two time points representing the displacement of a nucleus. Due to high imaging rate, the displacement of nuclei between subsequent time points at the chosen temporal resolution did not exceed half the average neighbour distance (see Supplementary Video 5 and Supplementary Fig. 6d). Therefore, the tracks could be constructed based on nearest neighbour point matching.

Pairs where identified by assigning each centroid to the spatially closest one in the previous time frame. Assuming a conserved number of points between subsequent frames, a perfect match may be achieved if the maximum distance travelled by a centroid during the time interval Δt is less than half the minimum distance between centroids at the same time point.

$$v_{max}(t)\Delta t < \frac{d_{min}(t)}{2} \tag{6}$$

In the experiments conducted here, the number of identified objects and thus the number of centroids changes over time. Potential sources for this are division, apoptosis or segmentation errors. Thus accurate segmentation is crucial for faithful nuclear track reconstruction. Apoptosis results in tracks ending, independent of the neighbouring nuclei. In case of divisions, a second round of assignments, mapping only the unassigned objects to the previous time point, was performed, yielding lineage relations between objects (Supplementary Fig. 6b-c and Supplementary Video 6). Finally, using the tracking information, we could calculate the average nucleus velocity (even during division), see Supplementary Fig. 6e and Supplementary Video 7.

Supplementary Fig. 6d shows the maximum displacement of the nuclei in one time-step $\Delta t = 25\ s$ and half of the minimal distance between neighboring nuclei as a function of time. The maximum displacement is below half the minimum distance between neighbors for most time points, which gives good conditions for point matching as

required by equation (6), confirming that our choice of temporal resolution for imaging. Shortly after divisions, the distance travelled exceeds half the minimum distance between nuclei. Nevertheless, tracking of objects and lineage tracing is still possible, as a collective motion of the nuclei without neighbour exchanges is observed.

From cycle 10 until early gastrulation, the distances between neighbouring cells' center of mass of does not exceed $d_{min} \approx 6\ \mu m$. Given our chosen temporal resolution, the lineage of cells may be reconstructed for any process, where the nuclei move with less than $v_{max} \approx 9\ \mu m/\text{min}$. A better temporal resolution - which may be readily achieved with our microscope - will allow for lineage tracing of objects that move even faster than $9\ \mu m/\text{min}$ or are closer than $6\ \mu m$, rendering our microscope ideally suited for the quantitative analysis of fast processes such as gastrulation, when cells move with speeds in the range of up to 6 μm/min (see Supplementary Fig. 6d).

Membrane analysis

To test the subcellular resolution capabilities of MuVi-SPIM, *Drosophila* embryos expressing gap43-mCherry[11] were imaged from cellularisation through to one hour after convergent extension. The Gap43-mCherry marker[11] allows visualization of the cell membrane. Imaging such a membrane marker enables exploration of cell shape changes and the corresponding forces during development[11,12]. Shortly after cellularisation the interface between cells is narrow, with a width of around 0.2-0.6 μm. Therefore, this was a good system for testing the subcellular resolution capabilities of MuVi-SPIM.

Drosophila development during the first three hours is highly dynamic. After cellularisation the embryo undergoes ventral furrow formation, cyphalic furrow formation and convergent extension. All these events occur in a short time window (less than one hour in total) and involve large-scale cell motion (see Supplementary Video 11). Though individual processes have been studied[13,14], it has thus far been impossible to gain a global understanding of how these different processes impact upon each other.

On a cellular level, individual cells undergo large deformations during this time; for example, cells are significantly elongated during ventral furrow formation[15]. How the embryo coordinates cellular motion on both local and global scales during this period is an open question, and has not been explored due to imaging limitations.

Membrane imaging fusion and segmentation are described in Methods. Having segmented the data, the time resolution was sufficiently fast to track many cells for over 20 minutes. Results of tracking are shown Supplementary Fig. 9c. Tracked nuclei are marked over a period of twenty minutes that overlaps with ventral and cephalic furrow formation. Using the tracking information, we calculated relevant biological quantities such as the cell velocity (Supplementary Fig. 9d). Ventral furrow formation results in rapid cell movement on the ventral side of the embryo (Supplementary Fig. 9d, arrow 1). However, at this time the rest of the embryo is unaffected. Around five minutes later the lateral sides begin to see large cell migration toward the ventral side (Supplementary Fig. 9d, arrow 2) followed, eventually, by dorsal cell motion around the embryo (Supplementary Fig. 9d, arrow 3). Cephalic furrow formation and convergent extension also result in large scale morphological changes (Supplementary Video 11).

During this period it becomes very difficult to track all cells since cell shape changes are rapid and many cells become internalised within the embryo.

Supplementary Protocol 1

Light-sheet alignment

Light-sheet alignment in previous SPIM implementations relied on small mirrors[16], which were inserted into the imaged volume such that the light-sheet was reflected directly into the imaging arm of the microscope. This method can only be used to align one light-sheet with a single detection arm at a time, and would therefore lead to slow and cumbersome microscope alignment if used in MuVi-SPIM. We have therefore developed a novel alignment protocol that allows simultaneous alignment of all four MuVi-SPIM arms and is executed faster than the standard alignment procedure even in a regular SPIM. Our method utilizes fluorescent aqueous solution in order to diagnose the microscope's alignment. Fluorescent solution can be obtained by mixing a soluble fluorophore (e.g. ATTO 532, ATTO-TEC) directly into the medium filled SPIM experimental chamber. Alternatively, the fluorescent solution can be sealed into a "fluorescent pouch" made of thin transparent polymer foil (e.g. BioFoil, In Vitro Systems & Services), to avoid fluorophore contamination of the experimental chamber and the objective lenses.

When such a fluorescent solution is illuminated through either of the illumination lens by a parked laser beam, this generates fluorescence emission confined to the volume of the beam. By taking a single image of such emission profile through the SPIM's detection arm, all three parameters important for accurate light-sheet alignment can be readily measured: position of the light-sheet relative to the detection arm's focal plane, position of the light-sheet's waist relative to the center of the detection field of view and lateral position of the illumination beam relative to the field of view. The latter defines the center of the scan range when the beam is scanned into a light-sheet. This method also allows one to easily evaluate if the light-sheet homogenously illuminates the field of view and the light-sheet's properties such as thickness and Rayleigh range.

Assuming completely misaligned MuVi-SPIM, the alignment procedure consists of the following steps (steps 1-6 for a regular SPIM):

1. While observing the experimental chamber from the top, the four objective lenses are first positioned such that the opposing objectives are pair-wise collinear and the distance between their front lenses correspond to twice their working distance.
2. Fluorescent solution is inserted into the imaged volume.
3. Fluorescent solution is illuminated by a parked laser beam through the first illumination arm. The waist of the beam is positioned in the middle between the detection lenses by readjusting their position.
4. The beam is then imaged through the first detection arm. Initially, no emission filter is used. The position of the beam can be inferred from the round shapes that are produced by the laser light scattered on particles floating through the beam (Supplementary Fig. 10a). With the use of the galvanometric scanner, beam is positioned into the detection arm's field of view.

5. The size of the circles produced by light scattering on the out-of-focus particles is then reduced by recursively adjusting the axial position of the active illumination and detection objective lens. If the circles move out of the field of view in the process, step 4 is repeated.
6. Once the scattered circles are confined to a narrow stripe along the beam, an emission filter is inserted, producing a well defined image of the laser beam (Supplementary Fig. 10b). By adjusting axial position of the active illumination objective lenses and the position of the active galvanometric scanner, the beam waist is brought to the center of the image (Supplementary Fig. 10c). Its lateral size is then minimized by adjusting the axial position of the active detection objective lens (Supplementary Fig. 10d).
7. The fluorescent medium is then illuminated through the second illumination arm. Steps 3-6 are repeated, but position of the first illumination objective lens and the first objective lens must be kept unchanged. The second laser beam is now brought into focus of the first detection arm by the galvanometric scanner, translating the beam in direction perpendicular to the focal plan of the detection lens until they both overlap. Again, once the emission filter is inserted, the second illumination arm should produce an image of a sharp laser beam with a waist in the middle of the image.
8. Finally, the fluorescent medium is illuminated through either of the illumination arms and imaged through the second detection arm. A sharp image of the beam with its waist in the middle of the image is then achieved by adjusting the second detection objective lens' position in axial and both lateral direction (a three-axis stage is required).
9. It is often useful to axially displace both light-sheets' waists, each in the direction towards its corresponding illumination lens[5] (Supplementary Fig. 10e). This can effectively increase the light-sheet's usable length up to a factor of two without increasing its thickness.

This procedure results in a setup where both light-sheets overlap with each other and with the both detection focal planes. The scanning range is set such that both light-sheets homogeneously illuminate the field of view (Supplementary Fig. 10f). The alignment can be fine-tuned with any specimen that demonstrates sharp features.

Supplementary Protocol 2

Diagnostic specimen preparation

The diagnostic specimen is a dispersion of fluorescent beads (Fluoersbrite multifluorescent 0.5µm beads 24054, Polysciences Inc.) diluted 1:1000 in 1% agarose solution (agarose N3103-0100, Starlab GmbH) at 80 ^{0}C. The dispersion is then sucked into a glass capillary (intraMARK BLAUBRAND, 100µl, cat. 708744, Brand GmbH). After the agarose polymerizes, the beads remain immobilized in the aqueous gel, a short segment of which is pushed out of the capillary and imaged in MuVi-SPIM.

Supplementary Protocol 3

Drosophila embryo preparation and mounting

Prior to mounting embryos are collected using apple-juice agar plates and dechorionated for 1-2 minutes in a fresh 50% bleach solution. Embryos are mounted in an agarose gel inside a glass micropipette, Supplementary Fig. 2b. We used 1% low melting agarose (StarPure Low Melt Agarose, cat. N3103-0100, StarLab GmbH), which was dissolved in a phosphate buffered saline (PBS) solution at 80^{0}C on a magnetic stirrer for six hours. The semifluid agarose gel is soaked into a disposable micropipette (intraMARK BLAUBRAND, 100µl, cat. 708744, Brand GmbH). The embryo is deposited into molten agarose gel with the embryo's long axis parallel to that of the micropipette. After the agarose polymerizes, a short segment of the gel cylinder is pushed out of the micropipette (Supplementary Fig. 2b). Thus, the embryo is held by the agarose gel alone, separated from the four objective lenses by nothing but water and aqueous gel. The mounting also allows for unconstrained 360^{0} of rotation around the embryo's long axis.

References

1. Saleh, B. E. A. & Teich, M. C. *Fundamentals of Photonics*. (Wiley & Sons: 2007).
2. Grill, S. & Stelzer, E. H. K. Method to calculate lateral and axial gain factors of optical setups with a large solid angle. *J. Opt. Soc. Am. A* **16**, 2658–2665 (1999).
3. Engelbrecht, C. J. & Stelzer, E. H. Resolution enhancement in a light-sheet-based microscope (SPIM). *Opt. Lett* **31**, 1477–1479 (2006).
4. Huisken, J., Swoger, J., Del Bene, F., Wittbrodt, J. & Stelzer, E. H. K. Optical Sectioning Deep Inside Live Embryos by Selective Plane Illumination Microscopy. *Science* **305**, 1007–1009 (2004).
5. Huisken, J. & Stainier, D. Y. R. Even fluorescence excitation by multidirectional selective plane illumination microscopy (mSPIM). *Opt. Lett.* **32**, 2608–2610 (2007).
6. Swoger, J., Verveer, P., Greger, K., Huisken, J. & Stelzer, E. H. K. Multi-view image fusion improves resolution in three-dimensional microscopy. *Opt. Express* **15**, 8029–8042 (2007).
7. Keller, P. J. *et al.* Fast, high-contrast imaging of animal development with scanned light sheet-based structured-illumination microscopy. *Nat Meth* **7**, 637–642 (2010).
8. Press, W. H., Teukolsky, S. A., Vetterling, W. T. & Flannery, B. P. *Numerical Recipes: The Art of Scientific Computing*. (Cambridge University Press: 2007).
9. Foe, V. E. & Alberts, B. M. Studies of nuclear and cytoplasmic behaviour during the five mitotic cycles that precede gastrulation in Drosophila embryogenesis. *Journal of Cell Science* **61**, 31–70 (1983).
10. Foe, V. E., Odell, G. M. & Edgar, B. A. Mitosis and Morphogenesis in the Drosophila Embryo: Point and Counterpoint. (1993).
11. Martin, A. C., Kaschube, M. & Wieschaus, E. F. Pulsed contractions of an actin-myosin network drive apical constriction. *Nature* **457**, 495–499 (2009).
12. Rauzi, M., Lenne, P.-F. & Lecuit, T. Planar polarized actomyosin contractile flows control epithelial junction remodelling. *Nature* **468**, 1110–1114 (2010).
13. Leptin, M. Gastrulation in Drosophila: the logic and the cellular mechanisms. *EMBO J* **18**, 3187–3192 (1999).
14. da Silva, S. M. & Vincent, J.-P. Oriented cell divisions in the extending germband of Drosophila. *Development* **134**, 3049 –3054 (2007).
15. Martin, A. C., Gelbart, M., Fernandez-Gonzalez, R., Kaschube, M. & Wieschaus, E. F. Integration of contractile forces during tissue invagination. *The Journal of Cell Biology* **188**, 735 –749 (2010).
16. Krzic, U. Multiple-view microscopy with light-sheet based fluorescence microscope. PhD Thesis, University of Heidelberg (2009)